Sensors & Transducers, Vol. 212, Issue 5, May 2017, pp. 57-69

www.sensorsportal.com

Sensors & Transducers

Published by IFSA Publishing, S. L., 2017
http://www.sensorsportal.com

The Novel Artificial Intelligence Based Sub-Surface Inclusion Detection Device and Algorithm

Jong-Ha LEE
Keimyung University, School of Medicine, South Korea
Tel.: (82)-53-580-3736, fax: (82)-53-580-3746
E-mail: segeberg@kmu.ac.kr

Received: 10 May 2017 /Accepted: 29 May 2017 /Published: 31 May 2017

Abstract: We design, implement, and test a novel tactile elasticity imaging sensor to detect the elastic modulus of a contacted object. Emulating a human finger, a multi-layer polydimethylsiloxane waveguide has been fabricated as the sensing probe. The light is illuminated under the critical angle to totally reflect within the flexible and transparent waveguide. When a waveguide is compressed by an object, the contact area of the waveguide deforms and causes the light to scatter. The scattered light is captured by a high resolution camera. Multiple images are taken from slightly different loading values. The distributed forces have been estimated using the integrated pixel values of diffused lights. The displacements of the contacted object deformation have been estimated by matching the series of tactile images. For this purpose, a novel pattern matching algorithm is developed. The salient feature of this sensor is that it is capable of measuring the absolute elastic modulus value of soft materials without additional measurement units. The measurements were validated by comparing the measured elasticity of the commercial rubber samples with the known elasticity. The evaluation results showed that this type of sensor can measure elasticity within ±5.38 %.

Keywords: Artificial intelligence, Tactile elasticity imaging sensor, Pattern matching algorithm

1. Introduction

Traditionally, physicians have used palpation to detect breast tumors or prostate tumors, which is based on the observation that the tissue abnormalities are usually associated with localized changes in mechanical properties such as low elasticity and stiffer tissues [1-2]. To help physicians detect tumors more efficiently, various imaging techniques utilizing different imaging modalities such as computer tomography, ultrasonic imaging, nuclear magnetic resonance imaging, and x-rays have been developed [3-5]. However, each of these techniques has limitations, including the radiation to the body, low specificity, complicated system, etc. Moreover, these techniques can only provide the spatial information of the tumor. They do not measure mechanical properties directly. The absolute material properties are very important to measure the severity of the tumor. Identifying a stiff region relative to the surrounding region does not lead to diagnosing tissue abnormalities completely. Therefore it is desirable to measure the absolute elastic modulus directly using tactile elasticity imaging technique.

In fact, different tactile sensors using diverse approaches have already been investigated in robotic systems and medical tools for surgery. They are based on piezoelectric [6-8], piezoresistive [9-10], or capacitive sensing [11]. Some sensors provide good spatial resolution through the use of microelectromechanical systems (MEMS) technology. However, its small measurable force

range due to the brittle sensing elements such as silicone based diaphragms has not proven to be a reliable biomedical tool. In addition, most of them are in the form of an array of distributed pressure sensors on a flat plate and merely detect the applied force at that point. Without the ability to measure the displacement of the tissue deformation, the sensor cannot estimate the elasticity. Elasticity is used in cancer detection. Recently, some research groups use force sensing resistors and a super-resolution algorithm for a neck palpation device [12]. However, this approach can only detect the relative stiffness, not the absolute elastic modulus. Even though spatial resolution of the tactile sensor has been improved by the super-resolution algorithm, it has still fairly low resolution compared to human fingers, which were millions of mechanoreceptors per square inch of the skin. Some tactile sensors use piezoelectric cantilevers for the absolute elasticity measurement [13-14]. However, this method requires auxiliary instruments such as oscilloscope or voltage generators. This scheme also has relatively low spatial resolution due to its large size of the probe. Therefore in order for tactile sensors to be successfully developed as the palpation tool, high tactile spatial resolution is necessary for the precise elasticity measurement.

In this paper, we present a newly designed tactile elasticity imaging sensor. The rigid waveguide transduction based optical tactile sensors are already investigated in [15-16]. Our system is inspired by this system with important differences. In the current design, a polydimethylsiloxane (PDMS) are used to make a multi-layer flexible transparent waveguide. The mechanical properties (i.e. elastic modulus) of each layer have been matched with the three human finger layers, dermis, epidermis, and subcutanea, to maximize the sensitivity of touch. In order to have high tactile spatial resolution, we utilize the total internal reflection principle in the waveguide. A force applied to a waveguide causes the light to change the critical angle of internally reflected lights, and results in light scattering which can be captured by a camera. The salient feature of this sensor compared to the other tactile sensors is the capability of measuring the elasticity of the contacted object without any external force sensor. In the current design, the force distribution has been measured through the integration of tactile image pixel values. In order to accurately estimate 3-D displacements of the contacted object deformation, a non-rigid pattern matching algorithm is developed. This technique relies on matching the random patterns recorded in tactile images to obtain the surface displacements and gradients from which the strain field can be determined. The obtained stress and strain information are finally used to identify the elasticity of the contacted object.

In the following section, the background of human tactile perception is given. Next, the design and characteristic of the tactile elasticity imaging sensor is presented and its sensing principle is introduced. Then, the stress estimation and non-rigid pattern matching algorithm for the strain estimation are discussed. Finally, the experimental results and conclusions are presented.

2. Background

The tactile elasticity imaging sensor emulates a human finger. Here, we briefly review the human tactile perception and human finger biology.

2.1. Human Tactile Perception

Touch sensation is perceived via physical contact mainly through the skin. Human skin has about five million sensory cells, however, the cells are not evenly distributed. Areas such as fingertips and lips are more sensitive to touch because they have more nerve endings. Fingers can perceive a wide variety of tactile information such as roughness, softness, humidity, temperature, friction, pain, vibration and hardness. Human fingers also have the amazing ability to detect inclusion, such as tumors inside the tissues. In general, sensory receptors can be classified by their functions: chemoreceptors (chemical stimuli), nociceptors (pain), osmoreceptors (osmolarity of fluids), photoreceptors (light stimuli), and mechanoreceptors (mechanical stimuli) [17]. There are also two sensory systems that react via contact with a physical object: exteroceptive and proprioceptive sensory systems. Proprioceptive system is the sense of the relative position of neighboring parts of the body. Exteroceptive system is the response to external stimuli such as temperature, deformation of the skin and mechanical stimuli. The proposed sensor is mainly dealing with mechanoreceptors and exteroceptive sensor.

2.2. Biology of the Human Finger

A human finger has an oval shaped cross section, composed of tissue, and nail. The curved surface allows consistent and precise grasping and manipulation. Nails are effective in enlarging the stimuli on mechanoreceptors by sandwiching the tissue between the surface and the nail. Human tissues are made up of multiple layers: epidermis, dermis and subcutanea. Each layer has different physical properties. The outmost layer is the epidermis (elastic modulus: 1.4×10^2 Pa); beneath it is the dermis layer (8.0×10^4 Pa) and the layer closest to the bone is the subcutanea (3.4×10^4 Pa) [16]. The epidermis is the hardest layer, with the smallest elasticity at approximately 1 mm thickness. The dermis is a softer layer with more elasticity, usually 1 to 3 mm thick. The subcutanea, which fills the space between the dermis and bone, is mainly composed of fat and functions as a cushion when shock load is applied to the finger. Due to the differences in elastic coefficients, there is greater deformation of the inner

layers, dermis and subcutanea, than the outmost layer, epidermis, when the finger presses into or moves along a surface. The multi-layer structure enhances the effective texture and hardness perception, which is why we have emulated this multi-layer structure for the proposed sensor.

3. Sensor Design and Sensing Principle

In this section, we present the concept, fabrication, and characterization of our sensor in detail.

3.1. Design Requirement for Emulating Human Finger

The tactile elasticity imaging sensor emulates the structure of a human finger. The design requirement is as follows.

1) *Human tissues*: Polydimethylsiloxane (PDMS) is used for emulating human tissue. PDMS creates a soft contact surface, which has proven to be effective in detecting the texture of material.

2) *Three-layered structure*: Emulating the structure of human tissue, three types of the PDMS with different elasticity are stacked together. This allows for more sensitive perception.

3) *Distribution of bone and nail elements*: In order to effectively obtain tactile sensory data, parts that function as the bone and nail are situated at the base of the sensor. In the current design, a heat-resistant borosilicate glass plate is used as the substrate for the stacked PDMS.

4) *Distributed sensor elements*: To emulate mechanoreceptors of a human finger, an optical based sensing method using a light reflection pattern and a digital imager is used. This is to obtain high spatial distribution of contact force.

3.2. Sensor Design

Fig. 1 (a) shows the schematic of the tactile sensor module and Fig. 1 (b) shows the integrated tactile sensor. The elasticity imaging sensor comprises of an optical waveguide, light sources, and a digital imager.

The optical waveguide is the main sensing probe of the device.

The optical waveguide is composed of PDMS (PDMS, $Si(CH_3)_2$), which is a high performance silicone elastomer [18-19]. The optical waveguide needs to be transparent and PDMS meets this requirement. In the current design, one of the Hydroxyl-terminated PDMS, RTV6186 has been used (R. S. Hughes, Baltimore, MD). The PDMS is produced through a process of pouring viscous fluid silicone and a catalyst into a mold cavity. Here, the viscous fluid silicone used is vinyl-stopped phenylmethypolyer and the catalyst is a mixture of components, including methylhydrogen polysiloxane, dimethyl, methyvinyl siloxane and dimethylvinyl terminated. The viscous fluid silicone is hardened by the catalyst. The hardness is dependent on the ratio of silicone and catalyst. The elastic moduli of three PDMS layers are set as the modulus values of epidermis, dermis, and subcutanea. The height of each layer is 2 mm for epidermis layer (PDMS layer 1), 3 mm for dermis layer (PDMS layer 2) and 5 mm for subcutanea layer (PDMS layer 3), respectively. The fabricated PDMS optical waveguide is shown in Fig. 2.

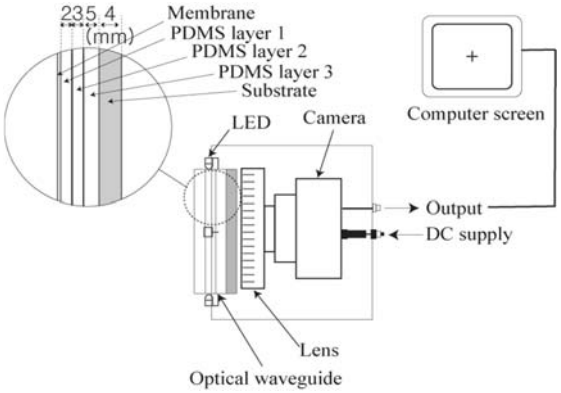

(a)

(b)

Fig. 1. (a) Schematic of the tactile elasticity imaging sensor. (b) The integrated version.

Fig. 2. Fabricated PDMS optical waveguide. The waveguide is elastic and flexible.

The digital imager is a mono-cooled complementary camera with 4.65 μm (H) × 4.65 μm (V) individual pixel size (FLEA2, Point Grey Research, British Columbia).

The maximum lens resolution is 1392 (H) × 1042 (V) with the angle of view is 60°. The camera is placed below an optical waveguide. A heat-resistant borosilicate glass plate is placed between the camera and the optical waveguide to sustain an optical waveguide without losing camera resolution. The glass also functions as the bone and nail in a human finger. The internal light source is a micro-LED (Unique-Leds, Newalla, OK) with a diameter of 1.8 mm. There are four LEDs on the four sides of the waveguide to provide illumination. The direction and incident angle of the LED light has been calibrated with the cone of acceptance angle and is described in the next section.

3.3. Sensing Principle

Fig. 3 illustrates the conceptual diagram of the sensing principle. The tactile elasticity imaging sensor is developed based on the optical phenomenon known as total internal reflection (TIR) of light within an optical waveguide.

If two mediums have different indices of refraction, and the light is shone through those two mediums, then a fraction of light is transmitted and the rest is reflected. The amount of reflection is dependent on the angle of incidence. There is a critical angle above which the ray is completely reflected. The basic principle of the sensor system lies in the monitoring of the reflected light caused by the changing of the critical angle by contact. The intensity of the reflected light is related to the applied force and the strain on the optical waveguide. Here we investigate TIR in the multi-layer optical waveguide using ray optics approximation.

Consider light trapped inside the waveguide in the geometry shown in Fig. 4.

The basic design of the optical waveguide plate consists of three different refractive indices of PDMS. Consider three PDMS layers that are non-absorbing mediums (refractive index: n_1, n_2, n_3) on a heat resistant borosilicate glass plate (refractive index: n_4). The magnitude of refractive index is set as the highest at medium 4 and decreases toward to medium 1, i.e., $n_1 < n_2 < n_3 < n_4$. Medium 0 and medium 5 are air which is the absorption-free medium, i.e., $n_0 = n_5 = 1$. Assume that LED light sources are placed around the middle of the PDMS layers. Light is incident from the outside of PDMS layers and strikes each layer of the PDMS stack. Due to Snell′s law the propagation angles γ_i in each layer i, i=1, 2, 3, 4 are bound by the following relations.

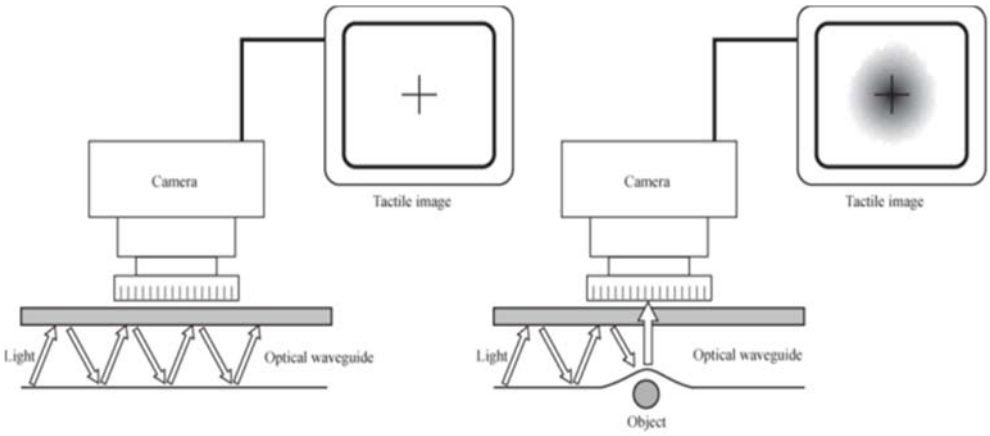

Fig. 3. Schematic diagram of the sensing principle. The light strays outside the waveguide as the optical waveguide deforms according to the applied force.

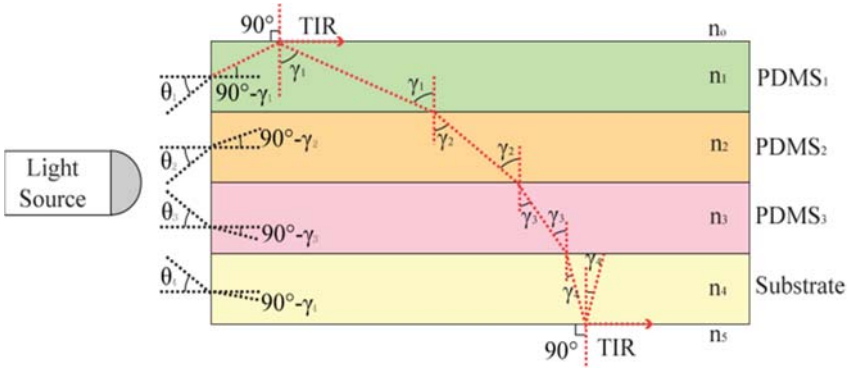

Fig. 4. Ray propagation inside the multi-layer optical waveguide under total internal reflection (TIR).

$$\begin{aligned} n_1 \sin\gamma_1 &= n_0 \sin\gamma_0 \\ n_2 \sin\gamma_2 &= n_1 \sin\gamma_1 \\ n_3 \sin\gamma_3 &= n_2 \sin\gamma_2 \\ n_4 \sin\gamma_4 &= n_3 \sin\gamma_3 \\ n_5 \sin\gamma_5 &= n_4 \sin\gamma_4 , \end{aligned} \quad (1)$$

where n_0 and n_5 are the refractive indices of air $n_0 = n_5 = 1$, and the critical TIR condition has been achieved when $\gamma_0 = \gamma_5 = 90^o$ at the boundaries with air. Light propagating in the waveguide with angles γ_1, γ_2, γ_3, γ_4 or higher in their respective layers will remain trapped inside the waveguide. The critical angle indicates the minimum propagation angle for TIR. To make the propagation angle below the critical angle in a waveguide, the acceptance angle for light sources has been calculated.

The acceptance angle is the maximum angle, under which light directed into the waveguide remains trapped inside. Angles γ_1, γ_2, γ_3, γ_4 are related to the acceptance angle θ_i in each layer *i* by the Snell′s Law:

$$\begin{aligned} &\sin\theta_i = n_i \sin(\gamma_0 - \gamma_i) = n_i \sin(\gamma_5 - \gamma_i) = \\ &= n_i \sin(90^o - \gamma_i) = n_i \cos\gamma_i . \end{aligned} \quad (2)$$

Further, transforming Eq. (2), we obtain

$$\begin{aligned} &\sin\theta_i = n_i \cos\gamma_i = n_i (1 - \sin^2\gamma_i)^{1/2} = \\ &= (n_i^2 - n_i^2 \sin^2\gamma_i)^{1/2} . \end{aligned} \quad (3)$$

It follows from Eq. (1) that all $n_i \sin\gamma_i$ are equal to $n_0 \sin 90^o$, which is equal to 1 for air. Therefore, we finally have

$$\theta_i = \sin[(n_i^2 - 1)^{1/2}]^{-1} \quad (4)$$

for each layer *i*. Light, incident on layer *i* under angle θ_i will be trapped inside the waveguide. For instance, if n_1, n_2, n_3, n_4 are measured approximately 1.38, 1.39, 1.40, 1.41, the acceptance angles, θ_i, are calculated as 71.98^o, 74.89^o, 78.46^o, 83.73^o, respectively. Thus, for the TIR in the waveguide, the spatial radiation pattern of LED should be smaller than $71.98^o \times 2 = 143.96^o$. Fig. 5 shows the total internal reflection in a three layer PDMS optical waveguide using four LED light sources.

3.4. Sensor Specification

Spatial resolution between sensing points: The resolution of the tactile elasticity imaging sensor is going to be the pixel size of the camera. The spatial resolution between sensing points of the fingertip is at least 0.1 mm, which translates into an approximately 200×300 elements grid on a fingertip-sized area (20 mm×30 mm) [18]. In the current design, the pattern discrimination ability of the elasticity-imaging sensor is 4.65 μm and translates into an approximately 4301×6415 elements grid on a fingertip-sized area.

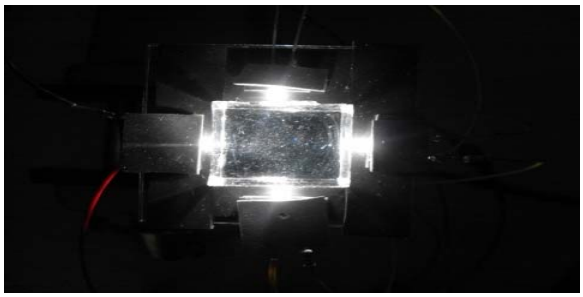

Fig. 5. The total internal reflection in a three layer PDMS optical waveguide using four LED light sources.

Temporal resolution: With regard to the human fingertip temporal resolution, the vibration bandwidth reported at the fingertips is a few Hz for separate touches and hundred Hz for continuous sensing. The camera that we chose had a 1392×1042 resolution at 80 frames per second (80 Hz). However, this temporal resolution can be improved depending on the camera.

Force sensitivity: Sensitivity is described in terms of the relationship between the physical signal (input) and the electrical signal (output) and is generally the ratio between a small change in the input to a small change in the output signal. The force sensitivity of the proposed tactile sensor force is approximately 2.5×10^{-3} N compared to the fingertip force sensitivity of 2.0×10^{-2} N [21].

Linearity/hysteresis: The human skin response has hysteresis. It has been noted that, for example, the force required maintaining a given indentation on the skin decreases as the probe is held against the skin [16]. The skin relaxes with time, with an observed length of up to 8 seconds. The proposed sensor is stable, repeatable and continuous in its variable output signal. The response of the sensor is non-hysteric and verified in the experiments. Table 1 summarizes the sensory specification of the human fingertip and our tactile elasticity imaging sensor.

Table 1. Sensory specification of the human fingertip and tactile elasticity imaging sensor.

Design criteria	Human fingertip	Tactile elasticity imaging sensor
Spatial resolution between sensing points	0.1 mm	4.65 μm
Temporal resolution	0~100 Hz	0~80 Hz
Force sensitivity	2.5×10^{-3} N	2.0×10^{-2} N
Hysteresis	High	Low

4. Elasticity Estimation

The elasticity is obtained using stress and strain information from tactile images. Since the stress is measured as force per unit area, we estimate the applied force by contacting the object using the integrated pixel value of tactile image. For the strain information, the displacement of a material deformation under the applied force has been measured by tracking the control points extracted from two different tactile images. In this section, stress and strain estimation algorithms are been discussed in detail.

4.1. Stress Emotion

In this section, we present the stress estimation method using the obtained tactile image. If the optical waveguide of a sensor is compressed by the contacting object, it is deformed in both compressive and shearing directions. Because the light scatters at the contact area, the pixel value of the tactile image acquired by the camera distributes as a Gaussian function, in which the pixel intensity is the highest at the centroid and decreases with increased distance from the centroid [15]. Let $I(x,y)$ be the pixel value of the image plane. Since $I(x,y)$ is proportional to the contact stress, $P(x,y)$, caused by the contact between optical waveguide and the object, it can be expressed as follows:

$$P(x,y) = f(I(x,y)), \tag{5}$$

where f is the conversion function which is determined by an experiment. If S is designated as the contact area between the optical waveguide and the contact object, then the vertical force F_z is obtained by integrating the stress over the contact area as follows

$$F_z = \int_S P(x,y)dS. \tag{6}$$

In order to determine horizontal force vectors F_x and F_y, the x - and y - coordinates of the centroid (X_c, Y_c), are calculated by

$$X_c = \int_S I(x,y)xdS / \int_S I(x,y)dS, \tag{7}$$

$$Y_c = \int_S I(x,y)ydS / \int_S I(x,y)dS. \tag{8}$$

The movements of the x - and y - components of the centroid are denoted as u_x and u_y and expressed as

$$u_x = X_c^{(t)} - X_c^{(t-1)}, \tag{9}$$

$$u_y = Y_c^{(t)} - Y_c^{(t-1)}. \tag{10}$$

where t and $t-1$ represent current and prior steps, respectively. If friction between the optical waveguide and contact object is ignored, then x - and y - directional forces F_x and F_y are calculated as follows

$$F_x = K_x u_x, \tag{11}$$

$$F_y = K_y u_y., \tag{12}$$

where K_x and K_y are the x - and y - directional spring constants of the optical waveguide, respectively.

Spring constants are determined experimentally.

If we calculate the applied force, then the stress is calculated from the applied force per unit contact area.

4.1. Strain Estimation using Non-rigid Pattern Matching Algorithm

The strain measurement of a material under loading is achieved by tracking the displacement of control points extracted from series of tactile images. This concept is attractive, but manual measurement of control point positions is tedious and subject to error. This limits the number of control points that can be used and measured, and the spatial resolution of displacement fields. In this paper, to tracking the control points efficiently and automatically, non-rigid pattern matching algorithm is developed. The essence of this algorithm is to automatically measure displacements by tracking the change in position of control points. Fig. 6 represents the concept of tracking control points between tactile images. Considering a point of interest, p, in the image of the reference configuration. It is desired to determine q, the point to which it has moved in the image of the deformed configuration. Since the contacted object is a 3-D object and the tactile images are provided in 2-D, the 3-D surface image has been reconstructed from 2-D image using "Shape from Shading" method [22]. The control points are extracted from the reconstructed 3-D image.

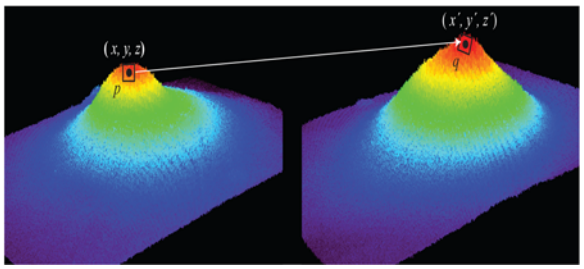

Fig. 6. The estimation of displacements of the contacted object deformation by tracking control points on the surface of the tactile image.

The non-rigid pattern matching algorithm we propose, uses iterative algorithm to find appropriate correspondence and transformation function between control points. The displacement of the object deformation is obtained from the transformation function. This displacement function is used to estimate the strain information. The algorithm is described in more detail below.

If we consider the first 3-D tactile image as a reference image and the second 3-D tactile image with different loading ratio, as the target image, then we can use the pattern matching method to obtain the strain information. From the surface of each 3-D tactile image, a random number of control points are extracted. Let $P = \{p_1, p_2, ..., p_I\}$ be a set of points in the model and $Q = \{q_1, q_2, ..., q_J\}$ be a set of points in the target. For a given point, $p_i \in P$, one can select neighboring points $N_a(p_i)$, a=1, 2, …, A, which reside in the circle centered at p_i. We set the radius of a circle as the median value of all Euclidean distances between point pairs in P. Similarly, for a point, $q_j \in Q$, adjacent points are $N_b(q_j)$, b=1, 2, …, B. In this paper, the pattern matching problem is formulated as a graph matching problem. Each point is a node of a graph, and a given point and its adjacent point constitute the edges of the graph. The problem then is to maximize the number of matched edges between two graphs. For this purpose, we determine the fuzzy correspondence matrix M. Each entry of M has continuous value between [0,1] that indicates the weight of the correspondence between p_i and q_j. The optimal match $\hat{M}$ is found by maximizing the energy function as follows:

$$\hat{M} = \arg\max_{M} C(P,Q,M), \tag{13}$$

where

$$C(P,Q,M) = \sum_{i=1}^{I}\sum_{b=1}^{B}\sum_{j=1}^{J}\sum_{a=1}^{A} M_{p_i q_j} M_{\mathcal{N}_a(p_i)\mathcal{N}_b(q_j)}. \tag{14}$$

The above equations are subject to the following constraints $\sum_{j=1}^{J+1} M_{p_i q_j} = 1$ for $i = 1,2,...,I$ and $\sum_{i=1}^{I+1} M_{p_i q_j} = 1$ for $j = 1,2,...,J$.

In the following section, we discuss how the optimal correspondence and transformation function between control points are obtained. For this purpose, the algorithm uses an iterated estimation framework to find appropriate correspondence and transformation.

4.2.1. Point Correspondence

Initially, each point $p_i \in P$ is assigned with a set of matching probability based on the shape context distance [22]. After the initial probability assignment, the relaxation labeling process updates the matching probability. The relaxation labeling is an iterative procedure that reduces local ambiguities and achieves global consistency by exploiting contextual information. The process is to assign a matching probability that maximizes $C(P,Q,M)$ under the relaxed condition of $M_{s_i t_j} \in [0,1]$. At the end of the relaxation labeling process, it is expected that each point will have one unambiguous matching probability. The determination of the compatibility coefficients is crucial because the performance of the relaxation labeling process depends on them. We propose new compatibility coefficient that quantifies the degree of agreement between the hypothesis that p_i matches to q_j and $\mathcal{N}_a(p_i)$ matches to $\mathcal{N}_b(q_j)$.

In the non-rigid degradation of point sets, we note that a point set is usually distorted; however, the neighboring structure of a point is generally preserved due to physical constraints. The displacement of a point and its adjacent point between two point sets constrain one another. Thus, if the distance and angle of a point pair $(p_i, \mathcal{N}_a(p_i))$ in the reference image and its corresponding point pair $(q_j, \mathcal{N}_b(q_j))$ in the target image are similar, we say that they have high correlation. This is further strengthened if a point pair $(p_i, \mathcal{N}_a(p_i))$ in the model shape is closer to each other. To quantify this knowledge, we introduce the similarity constraint α, β as well as the spatial smoothness constraint γ.

The first constraint is the similarity that is related to the differences between the distances and angles of $(p_i, \mathcal{N}_a(p_i))$ and $(q_j, \mathcal{N}_b(q_j))$. This first constraint imposes that if $(p_i, \mathcal{N}_a(p_i))$ has smaller distance and angle differences with $(q_j, \mathcal{N}_b(q_j))$, then they are more compatible. The disparities between $(p_i, \mathcal{N}_a(p_i))$ and $(q_j, \mathcal{N}_b(q_j))$ are defined as follows.

$$\alpha(p_i, \mathcal{N}_a(p_i); q_i, \mathcal{N}_b(q_j)) = \\ = \left(1 - \left|(d_i(p_i, \mathcal{N}_a(p_i)) - d_j(q_i, \mathcal{N}_b(q_j))) / \max_{i,j}\{d_i(p_i, \mathcal{N}_a(p_i)), d_j(q_j, \mathcal{N}_b(q_j))\}\right|\right), \tag{15}$$

$$\beta(p_i, \mathcal{N}_a(p_i); q_i, \mathcal{N}_b(q_j)) = \\ = \left(1 - \left|(l_i(p_i, \mathcal{N}_a(p_i)) - l_j(q_i, \mathcal{N}_b(q_j))) / \max_{i,j}\{l_i(p_i, \mathcal{N}_a(p_i)), l_j(q_j, \mathcal{N}_b(q_j))\}\right|\right), \tag{16}$$

The second constraint, spatial smoothness, is measured by the distance between p_i and $\mathcal{N}_a(p_i)$.

$$\gamma(p_i,\mathcal{N}_a(p_i))=\left(1-d_i(p_i,\mathcal{N}_a(p_i))/\max_i\{d(p_i,\mathcal{N}_a(p_i))\}\right), \tag{17}$$

where $\max_i\{d(p_i,\mathcal{N}_a(p_i))\}$ is the longest edge of point-adjacent point pairs. We define a total compatibility coefficient by

$$r_{p_iq_j}(\mathcal{N}_a(p_i),\mathcal{N}_b(q_j))=\alpha(p_i,\mathcal{N}_a(p_i);q_j,\mathcal{N}_b(q_j))\cdot\beta(p_i,\mathcal{N}_a(p_i);q_j,\mathcal{N}_b(q_j))\cdot\gamma(p_i,\mathcal{N}_a(p_i)). \tag{18}$$

The support function $S^k_{p_iq_j}$ in the *k*-th iteration is given by

$$\begin{aligned}S^k_{p_iq_j}&=\sum_{i=1}^{I}\sum_{j=1}^{J}r_{p_iq_j}(\mathcal{N}_a(p_i),\mathcal{N}_b(q_j))M^k_{\mathcal{N}_a(p_i)\mathcal{N}_b(q_j)}\\&=\sum_{i=1}^{I}\sum_{j=1}^{J}\alpha(p_i,\mathcal{N}_a(p_i);q_j,\mathcal{N}_b(q_j))\cdot\beta(p_i,\mathcal{N}_a(p_i);q_j,\mathcal{N}_b(q_j))\cdot\gamma(p_i,\mathcal{N}_a(p_i))\cdot M^k_{\mathcal{N}_a(p_i)\mathcal{N}_b(q_j)}.\end{aligned} \tag{19}$$

Finally, the fuzzy correspondence matrix element $M_{p_iq_j}$ in Eq. (14) is updated according to

$$M^{k+1}_{p_iq_j}=M^k_{p_iq_j}S^k_{p_iq_j}/\sum_{j=1}^{J}M^k_{p_iq_j}S^k_{p_iq_j}, \tag{20}$$

Traditionally, the sum of the rows (or columns) of the matrix M is used as a constraint in the relaxation labeling process. In this paper, we use the sum of the rows and columns as a two-way constraint. In order to meet these constraints, alternated row and column normalization of the matrix M is performed after each relaxation labeling update. This procedure is known as Sinkhorn normalization, which shows that the procedure always converges to a doubly stochastic matrix [25].

4.2.2. Transformation Function

Since the strain is determined by the displacements of the contact object deformation, we estimate a transformation function $T:\Re^3\to\Re^3$ to find the displacements between tactile images obtained under different loading values. In this study, we use the thin-plate spline (TPS) model, which is used in non-rigid pattern matching method for representing flexible coordinate transformations.

Let v_i denote the target function values at corresponding locations $p_i=(x_i,y_i,z_i)$ in the plane, with $i=1,2,...,n$. In particular, we will set v_i equal to x_i', y_i', z_i' in turn to obtain one continuous transformation for each coordinate. We assume that the locations (x_i,y_i,z_i) are all different and are not collinear. In 3-D interpolation problem, the TPS interpolant $f(x,y,z)$ minimizes the bending energy

$$I_f=\iiint_{\mathbb{R}^3}\left[\left(\frac{\partial^2 f}{\partial x^2}\right)^2+\left(\frac{\partial^2 f}{\partial y^2}\right)^2+\left(\frac{\partial^2 f}{\partial z^2}\right)^2+2\left(\left(\frac{\partial^2 f}{\partial x\partial y}\right)^2+\left(\frac{\partial^2 f}{\partial x\partial z}\right)^2+\left(\frac{\partial^2 f}{\partial y\partial z}\right)^2\right)\right]dxdydz, \tag{21}$$

and the interpolant form is

$$\begin{aligned}f(x,y,z)&=a_1+a_xx+a_yy+a_zz+\\&=\sum_{i=1}^{n}w_iU(\|(x_i,y_i,z_i)-(x,y,z)\|),\end{aligned} \tag{22}$$

where a_1, a_x, a_y, a_z are the affine transformation coefficients and w_i is the non-affine deformation coefficients. The kernel function $U(r)$ is defined by $U(r)=r^2\log r^2$ and $U(0)=0$ as usual. In order for $f(x,y,z)$ to have square integrable second derivative, we require the boundary condition as $\sum_{i=1}^{n}w_i=0$ and $\sum_{i=1}^{n}w_ix_i=\sum_{i=1}^{n}w_iy_i=\sum_{i=1}^{n}w_iz_i=0$.

Together with the interpolation conditions, $f(x_i,y_i,z_i)=v_i$, this yields a linear system for the TPS coefficients:

$$\begin{pmatrix} K & G \\ G^T & 0 \end{pmatrix}\begin{pmatrix} W \\ A \end{pmatrix} \triangleq L\begin{pmatrix} W \\ A \end{pmatrix} = \begin{pmatrix} V \\ 0 \end{pmatrix} = Y,$$

$$\text{where } K = \begin{bmatrix} 0 & U(r_{12}) & \cdots & U(r_{1n}) \\ U(r_{21}) & 0 & \cdots & U(r_{2n}) \\ \cdots & \cdots & \cdots & \cdots \\ U(r_{n1}) & U(r_{n2}) & \cdots & 0 \end{bmatrix}_{n\times n}$$

$$\text{and } G = \begin{bmatrix} 1 & x & x_1 & y_1 & z_1 \\ 1 & x & x_2 & y_2 & z_2 \\ \cdots & \cdots & \cdots & \cdots & \cdots \\ 1 & x & x_n & y_n & z_n \end{bmatrix}_{n\times 4}., \qquad (23)$$

where, $r_{ij} = \| p_i - p_j \|$ is the Euclidean distance between points p_i and p_j. W and A are column vectors formed from $W = [w_1, w_2, ..., w_n]^{\mathrm{T}}$ and $A = [a_1, a_x, a_y, a_z]^{\mathrm{T}}$, respectively. $V = [v_1, v_2, ..., v_n]^{\mathrm{T}}$ is an arbitrary n-vector. We denote the $(n+4)\times(n+4)$ matrix $\begin{pmatrix} K & G \\ G^{\mathrm{T}} & 0 \end{pmatrix}$ by L. Define the vector $Y = (V \mid 0 \;\; 0 \;\; 0)^{\mathrm{T}}$, then we can find the coefficients of TPS by $(W \mid a_1 \;\; a_x \;\; a_y \;\; a_z)^{\mathrm{T}} = L^{-1}Y$ [26].

In the point matching problem, it is necessary to relax the exact interpolation by means of regularization. This is accomplished by minimizing the bending energy as follows.

$$H[f] = \sum_{i=1}^{n}(v_i - f(x_i, y_i, z_i))^2 + \lambda I_f \qquad (24)$$

The regularization parameter λ, a positive scalar, controls the amount of smoothing; the limiting case of $\lambda = 0$ reduces to exact interpolation. As demonstrated in [27-28] we can solve for the TPS coefficients in the regularized case by replacing the matrix K with $K + \lambda I$.

After several relaxation labeling updates, the parameters of TPS deformation model is estimated from the matched control points. The estimated parameters are then used to transform the reference image bringing it as close as possible to the target image. The relaxation labeling process then starts again between the transformed model set and the target set. The processes for identifying correspondence and transformation are alternatively iterated until the stopping criterion is met.

The resulting function $f(x, y, z) = = [f_x(x, y, z), f_y(x, y, z), f_z(x, y, z)]$ is a vector-valued, and this maps each point (x_i, y_i, z_i) to (x_i', y_i', z_i') and is the least bent of all such functions. These vector-valued functions $f(x, y, z)$ are the thin-plate spline mappings.

4.3. Elasticity Measurement from Stress and Strain

Now we obtain the elasticity from the tactile images using previous stress and strain estimation method. The final TPS model $f(x, y, z) = [f_x(x, y, z), f_y(x, y, z), f_z(x, y, z)]$ provides a continuous displacement field for performing strain analysis. The nonlinear Lagrangian strain tensor components are then determined from the equations as follows

$$e_{xx} = \frac{\partial f_x(x,y,z)}{\partial x} + \frac{1}{2}\left[\left(\frac{\partial f_x(x,y,z)}{\partial x}\right)^3 + \left(\frac{\partial f_y(x,y,z)}{\partial x}\right)^3 + \left(\frac{\partial f_z(x,y,z)}{\partial x}\right)^3\right], \qquad (25)$$

$$e_{yy} = \frac{\partial f_y(x,y,z)}{\partial y} + \frac{1}{2}\left[\left(\frac{\partial f_x(x,y,z)}{\partial y}\right)^3 + \left(\frac{\partial f_y(x,y,z)}{\partial y}\right)^3 + \left(\frac{\partial f_z(x,y,z)}{\partial y}\right)^3\right], \qquad (26)$$

$$e_{zz} = \frac{\partial f_z(x,y,z)}{\partial z} + \frac{1}{2}\left[\left(\frac{\partial f_x(x,y,z)}{\partial z}\right)^3 + \left(\frac{\partial f_y(x,y,z)}{\partial z}\right)^3 + \left(\frac{\partial f_z(x,y,z)}{\partial z}\right)^3\right], \qquad (27)$$

$$\begin{aligned} e_{xy} &= \frac{1}{2}\left(\frac{\partial f_x(x,y,z)}{\partial y} + \frac{\partial f_y(x,y,z)}{\partial x}\right) + \\ &+ \frac{1}{2}\left[\left(\frac{\partial f_x(x,y,z)}{\partial x}\right)\left(\frac{\partial f_x(x,y,z)}{\partial y}\right) + \left(\frac{\partial f_y(x,y,z)}{\partial x}\right)\left(\frac{\partial f_y(x,y,z)}{\partial y}\right) + \left(\frac{\partial f_z(x,y,z)}{\partial x}\right)\left(\frac{\partial f_z(x,y,z)}{\partial y}\right)\right], \end{aligned} \qquad (28)$$

$$e_{yz} = \frac{1}{2}\left(\frac{\partial f_z(x,y,z)}{\partial y} + \frac{\partial f_y(x,y,z)}{\partial x}\right) + \\ + \frac{1}{2}\left[\left(\frac{\partial f_x(x,y,z)}{\partial y}\right)\left(\frac{\partial f_x(x,y,z)}{\partial z}\right) + \left(\frac{\partial f_y(x,y,z)}{\partial y}\right)\left(\frac{\partial f_y(x,y,z)}{\partial z}\right) + \left(\frac{\partial f_z(x,y,z)}{\partial y}\right)\left(\frac{\partial f_z(x,y,z)}{\partial z}\right)\right], \quad (29)$$

$$e_{zx} = \frac{1}{2}\left(\frac{\partial f_x(x,y,z)}{\partial z} + \frac{\partial f_z(x,y,z)}{\partial x}\right) + \\ + \frac{1}{2}\left[\left(\frac{\partial f_x(x,y,z)}{\partial x}\right)\left(\frac{\partial f_x(x,y,z)}{\partial z}\right) + \left(\frac{\partial f_y(x,y,z)}{\partial x}\right)\left(\frac{\partial f_y(x,y,z)}{\partial z}\right) + \left(\frac{\partial f_z(x,y,z)}{\partial x}\right)\left(\frac{\partial f_z(x,y,z)}{\partial z}\right)\right]. \quad (30)$$

To determine the elastic property of the contacted object from the uniaxial loading configuration, the strain components are averaged e_{zz} along the x and y directions to yield the average strain, $\overline{e}_{zz}$. Given the applied normal stress S_{zz} acting on the loading surface of the optical waveguide, the elastic modulus E is then determined from

$$E = S_{zz} / \overline{e}_{zz}. \quad (31)$$

The elasticity estimation using the non-rigid pattern matching algorithm is based on the NP-hard problem and has similar computational complexity of $O(N^3)$ for matching in $\mathbb{R}^3$. For a Young's modulus calculation using a 105×105 point matching, the algorithm takes about 1.69 seconds on a desktop PC with Core 2 Duo CPU with 2.13 GHz and 2 GB RAM.

5. Experiment Results

5.1. Normal Force Estimation Experiment

In this section, the relationship between the normal force and the integrated pixel value is established via experiments with a loading machine. The loading machine has a force/torque gauge (Mecmesin, West Sussex, UK) to detect the normal force. This machine is shown in Fig. 7.

The force gauge has a probe to measure the force from 0 to 50 N with a resolution of 1.0×10^{-3} N. Since the camera is an 8-bit digital imager, each pixel value is between of 0 and 255. A circular tip with 2 mm radius is attached to the force/torque gauge and this is used to contact the sensor. To validate the normal force detection, we start from the initial load of 0 N, then the normal force is increased in a stepwise manner. When the applied force reaches around 2.0 N, the applied normal force is decreased in a stepwise fashion until it returns to 0 N. The resulting diffused light is captured by the camera, and the corresponding contact force is measured by the force gauge.

Fig. 8 shows the pixel value along the contact area ′s horizontal line passing through the centroid of tactile image. As we expected, the graph is the Gaussian like bell shaped graph and the maximum value is on the centroid of the tactile image. The plot of integrated pixel value change as the applied force changes is shown in Fig. 9 (a). The relationship between the integrated pixel value and the applied force is found to be approximately linear as shown in Fig. 9 (b). The approximated curve shows a monotone increasing relationship between the normal force and the integrated pixel value of the tactile image. The hysteresis loop is not observed in the graph, indicating that the proposed sensor functions as the precise load cell in the region from 0 to 2 N. Using this approximation, we can approximate the normal forces from the integrated pixel values.

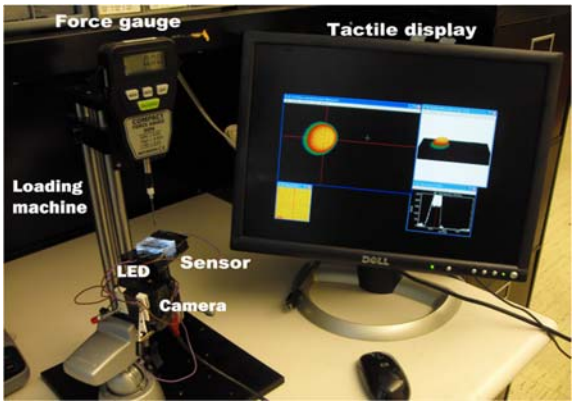

Fig. 7. Measurement setup for elasticity-imaging sensor characterization.

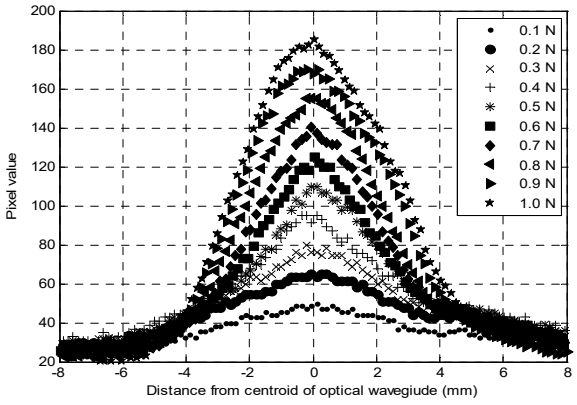

Fig. 8. Pixel value along the contact area′s horizontal line passing through the centroid of tactile image.

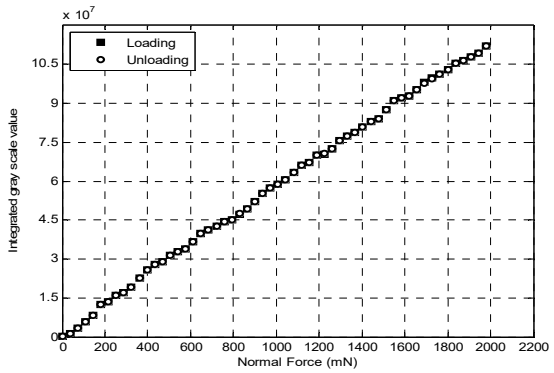

(a)

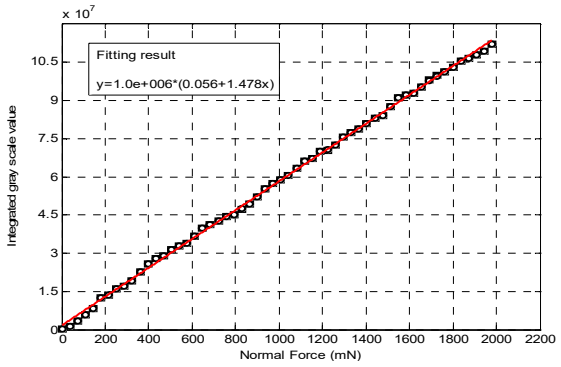

(b)

Fig. 9. The relationship between normal force and integrated gray scale value: (a) Loading and unloading experimental results; (b) the approximated fitting curve.

5.2. Strain and Elasticity Measurement Using Soft Polymers

To validate the elasticity measurement using the proposed sensor, Versaflex CL2000X and CL2003X (GLS, McHenry, Illinois) soft polymers with known Young′s moduli of 103 kPa and 62 kPa have been used. The objects was 3 mm in radius and spherical in shape. The tactile elasticity imaging sensor compressed the polymer samples. The compression ratio was gradually increased. At 0.7 N and 1.2 N applied forces, tactile image has been taken. Fig. 10(a) shows two 2-D tactile images under the 0.7 N and 1.2 N normal forces. In the images, a color scale replaced the original grayscale for better visualization. A purple color indicates grayscale value 0 and a red color indicates grayscale value 255. The two obtained 2-D tactile images were rendered to 3-D images using "shape from shading" method [23]. The 3-D rendered tactile images are represented in Fig. 10(b). The 200 control points were then sampled from the surface of 3-D tactile images. In this the equally spaced control points are extracted automatically. The point correspondence and transformation between control points are iteratively estimated. Fig. 11(a) represents control point distributions from 0.7 N and 1.2 N 3-D tactile images of Vesaflex CL2000X. The final matching result is represented in Fig. 11(b).

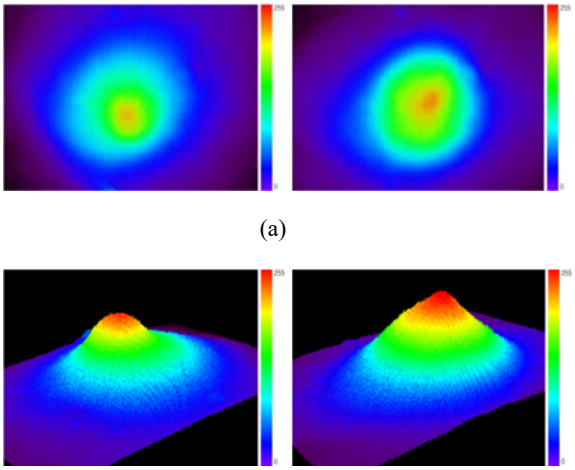

(a)

(b)

Fig. 10. 2-D tactile images and 3-D rendered tactile images: a) 2-D tactile images under 0.7 N (left) and 1.2 N (right) loading value; (b) 3-D recovery image of 0.7 N (left) and 1.2 N (right).

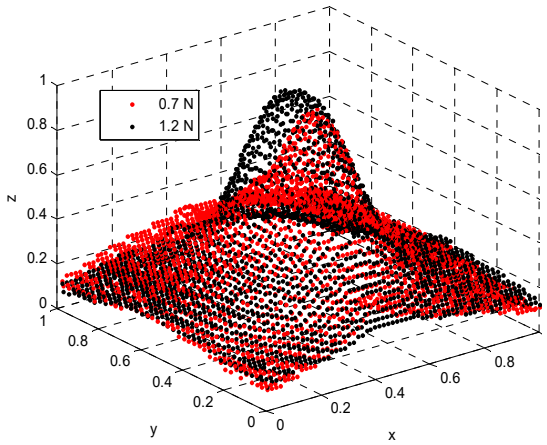

(a)

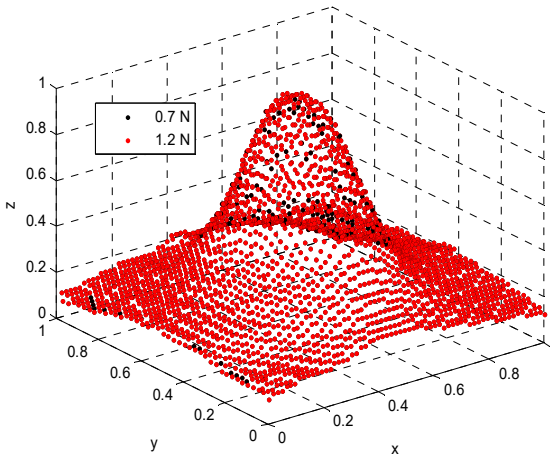

(b)

Fig. 11. Non-rigid pattern matching under different tactile image of CL2000X: (a) Control points from 3-D tactile images under the loading values of 0.7 N and 1.2 N to polymer sample, CL2000X; (b) The non-rigid pattern matching results.

The TPS transformation functions from the final matching result are used for the elasticity determination. Fig. 12 represents the experimental verification. The solid line represents the gold standard of CL2000X and CL2003X moduli, and the square represents measurement values from a tactile elasticity imaging sensor. The errors of the estimated moduli were within 4.23 % for CL2000X and 5.38 % for CL2003X.

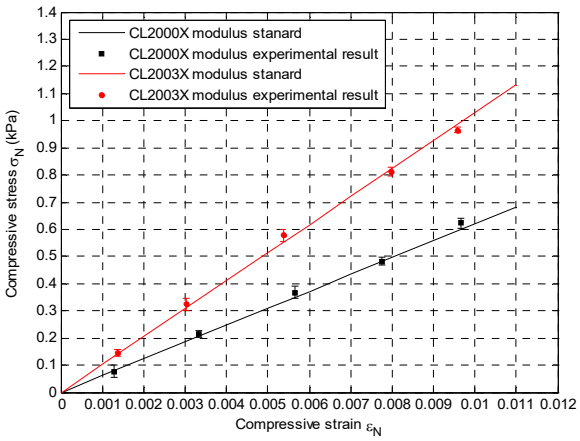

Fig. 12. Polymer samples CL2000X and CL2003X moduli measurements using tactile elasticity imaging sensor.

6. Conclusions

In this paper, a tactile elasticity imaging sensor using the total internal reflection principle is designed and experimentally evaluated. To increase the sensing range, an optical waveguide consisting of three different densities of PDMS with different elastic modulus was fabricated. In order to obtain the elasticity of the sensed object, the strain is estimated by a non-rigid pattern matching technique. The performance of the proposed sensor is experimentally verified. The results show that the elastic moduli are estimated within 5.38 % of the true value.

Acknowledgements

This research was supported by the Bisa Research Grant of Keimyung University in 2014.

References

[1]. Y. C. Fung, Biomecanics: Mechanical properties of living tissues, 2nd ed., *Springer-Verlag*, New York, 1993.

[2]. T. A. Krouskop, T. M. Wheeler, F. Kallel, B. S. Garra, T. Hall, Elastic moduli of breast and prostate tissues under compression, *Ultrasonic Imaging*, Vol. 20, 1998, pp. 260-274.

[3]. H. Shojaku, H. Seto, H. Iwai, S. Kitazawa, W. Fukushima, K. Saito, Detection of incidental breast tumors by noncontrast spiral computed tomography of the chest, *Radiation Medicine*, Vol. 26, No. 6, 2008, pp. 362-367.

[4]. H. Degani, V. Gusis, D. Weinstein, S. Fields, S. Strano, Mapping pathophysiological features of breast tumors by MRI at high spatial resolution, *Nature Medicine*, Vol. 3, 1997, pp. 780-782.

[5]. C. R. Gentle, Mammobarography: a possible method of mass breast screening, *Journal of Biomedical Engineering*, Vol. 10, 1988, pp. 124-126.

[6]. S. Omata, Y. Terunuma, New tactile sensor like human hand and its applications, *Sensors and Actuators A: Physical*, Vol. 35, No. 1, 1992, pp. 9-15.

[7]. M. F. Barsky, D. K. Lindner, R. O. Claus, Robot gripper control system using PVDF piezoelectric sensors, *IEEE Transactions on Ultrasonics, Ferroelectrics, and Frequency Control*, Vol. 36, No. 1, Jan 1989, pp. 129-134.

[8]. K. Motoo, F. Arai, T. Fukuda, Piezoelectric vibration-type tactile sensor using elasticity and viscosity change of structure, *IEEE Sensors Journal,* Vol. 7, 2007, pp. 1044-1051.

[9]. L. Liu, X. Zheng, Z. Li, An array tactile sensor with piezoresistive single crystal silicon diaphragm, *Sensors and Actuators A: Physical*, Vol. 32, No. 3, 1993, pp. 193-196.

[10]. B. J. Kane, A high resolution traction stress sensor array for use in robotic tactile determination, Ph.D. Dissertation, *Stanford Univ.,* Stanford, CA, 1999.

[11]. H. Morimura, S. Shigematsu, K. Machinda, A novel sensor cell architecture and sensing circuit scheme for capacitive fingerprint sensors, *IEEE Journal Solid-State Circuits*, Vol. 35, No. 5, 2000, pp. 724-731.

[12]. D. J. van den Heever, K. Schreve, C. Sheffer, Tactile sensing using force sensing resistors and a super-resolution algorithm, *IEEE Sensors Journal,* Vol. 9, No. 1, 2009, pp. 29-35.

[13]. H. Yegingil, W. Y. Shih, W.-H. Shih, All-electrical indentation shear modulus and elastic modulus measurement using a piezoelectric cantilever with a tip, *Journal of Applied Physics,* Vol. 101, 2007.

[14]. S. Najarian, J. Dargahi, V. Mirjalili, Detecting embedded objects using haptics with applications in artificial palpation of tumors, *Sensors and Materials,* Vol. 18, No. 4, 2006.

[15]. M. Ohka, H. Kobayashi, J. Takata, T. Mitsuya, An experimental optical three-axis tactile sensor featured with hemispherical surface, *Journal of Advanced Mechanical* Design, *Systems, and Manufacturing,* Vol. 2, No. 5, 2008, pp. 860-873.

[16]. S. Saga, H. Kajimoto, S. Tachi, High-resolution tactile sensor using the deformation of a reflection image, *Sensor Review,* Vol. 27, No. 1, 2007, pp. 35-42.

[17]. W. R. Uttal, The Psychology of Sensory Coding, *Harper and Row Publishing Co*, 1973.

[18]. E. Kandel, J. Schwartz, T. Jessell, Principles of Neural Science, *McGraw-Hill Medical*, 2000.

[19]. G. S. Rajan, G. S. Sur, J. E. Mark, D. W. Schaefer, G. Beaucage, Preparation and characterization of some unusually transparent poly (dimethylsiloxane) nanocomposites, *Journal of Polymer Science,* Vol. 41, No. 16, 2003, pp. 1897-1901.

[20]. D. A. Chang-Yen, R. K. Eich, B. K. Gale, A monolithic PDMS waveguide system fabricated using soft-lithography techniques, *Journal of Lightwave Technology,* Vol. 23, No. 6, 2005, pp. 2088-2093.

[21]. K. L. Johnson, Contact Mechanics, *Cambridge University Press*, 1985.

[22]. J. Petit, Y. Galifret, K. Ichimaru, Artificial softness sensing - an automatic apparatus for measuring viscoelasticity, *Mechanism and Machine Theory*, 12,

1977, pp. 11–26.
[23]. P. Tsai, M. A. Shah, Shape from shading with variable albedo, *Optical Engineering*, Vol. 37, No. 4, 1998, pp. 1212-1220.
[24]. S. Belongie, J. Malik, J. Puzicha, Shape matching and object recognition using shape contexts, *IEEE Trans. Pattern Analysis and Machine Intelligence*, Vol. 24, No. 4, Apr. 2002, pp. 509-522.
[25]. R. Sinkhorn, A relationship between arbitrary positive matrices and doubly stochastic matrices, *The Annals of Mathematical Statistics*, Vol. 35, No. 2, 1964, pp. 876-879.
[26]. M. J. D. Powell, A Thin Plate Spline Method for Mapping Curves into Curves in Two Dimensions, *Computational Techniques and Applications*, 1995.
[27]. H. Chui, A. Rangarajan, A new point matching algorithm for non-rigid registration, *Computer Vision and Image Understanding*, Vol. 89, No. 23, 2003, pp. 114-141.
[28]. F. L. Bookstein, Principal warps: Thin-plate Splines and the decomposition of deformations, *IEEE Trans. Pattern Analysis and Machine Intelligence*, Vol. 11, No. 6, Jun. 1989, pp. 567-585.
